IEEE Open Journal of
Antennas and Propagation

Received 16 December 2021; revised 12 January 2022; accepted 13 January 2022. Date of publication 18 January 2022; date of current version 1 February 2022.

Digital Object Identifier 10.1109/OJAP.2022.3143993

Dual-Polarized 2–6 GHz Antenna Array With Inverted BoR Elements and Integrated PCB Feed

MATTI KUOSMANEN[1,2], STEN E. GUNNARSSON[3] (Senior Member, IEEE), JOHAN MALMSTRÖM[3], HENRI KÄHKÖNEN[1,2], JARI HOLOPAINEN[1], JUHA ALA-LAURINAHO[1], AND VILLE VIIKARI[1] (Senior Member, IEEE)

[1]Department of Electronics and Nanoengineering, Aalto University, 02150 Espoo, Finland

[2]Saab Surveillance, Saab Finland Oy, 00100 Helsinki, Finland

[3]Saab Surveillance, Saab AB, 175 88 Järfälla, Sweden

CORRESPONDING AUTHOR: M. KUOSMANEN (e-mail: matti.s.kuosmanen@aalto.fi)

This work was supported by Saab AB.

ABSTRACT This article presents a wideband, dual-polarized antenna array with inverted BoR elements. The antenna structure is based on the conventional body-of-revolution (BoR) element, but the structure is inverted; i.e., instead of metallic cones, the elements are metalized cavities inside a dielectric block. This structure allows a more lightweight and low-cost design since all-metal parts are not needed. In addition to the inverted BoR structure, this paper proposes a feeding system that is fully integrated into a 5-mm-thick standard printed circuit board. The designed antenna operates at 2–6 GHz, providing 3:1 impedance bandwidth with an active reflection coefficient (ARC) < -10 dB. The ARC<-10 dB criterion is fulfilled for all beam-steering angles up to $\pm 50^{\circ}$ in all planes. The operation of the simulated antenna array was verified by measuring a built prototype. The measurement results are in good agreement with the simulations. However, the radiation efficiency of the prototype was approximately 11% inferior than that of the conventional all-metal BoR array due to conduction losses caused by the metalization of the used dielectric.

INDEX TERMS Antenna array, BoR, flared-notch antenna, phased array, tapered slot, Vivaldi antenna, wideband, low cost, low weight.

I. INTRODUCTION

MODERN needs for communication and sensing applications place increasingly stricter requirements on antennas. The development of the technology has led to systems that can be used for various applications, such as communication and sensing. Communication systems need a large bandwidth since the number of communication technologies is constantly growing, thus increasing the ranges of different frequency bands. Passive sensing applications, in turn, are inherently wideband due to their need to sense a large variety of signals from the environment.

For these purposes, wideband antenna arrays are a good option. They are particularly suitable since the radiation energy can be efficiently directed towards another transmitting or receiving antenna. Furthermore, the ability to steer the antenna beam allows finding targets accurately in sensing systems. Suitable arrays for these purposes have been used in military applications for a long time. For example, phased arrays have become the most common antenna type in newer high-performance radars. Wideband phased arrays, in turn, are used in electronic warfare (EW), where directive, beam-steerable arrays are required for passive sensing and jamming. However, these arrays are often heavy and expensive due to extreme requirements for durability and reliability.

A common choice to implement a wideband antenna array is to use Vivaldi (i.e., tapered slotline) elements [1]. They have been extensively studied in the last few decades since they offer a simple structure and scalable wideband operation. More recently, a number of different array

This work is licensed under a Creative Commons Attribution 4.0 License. For more information, see https://creativecommons.org/licenses/by/4.0/

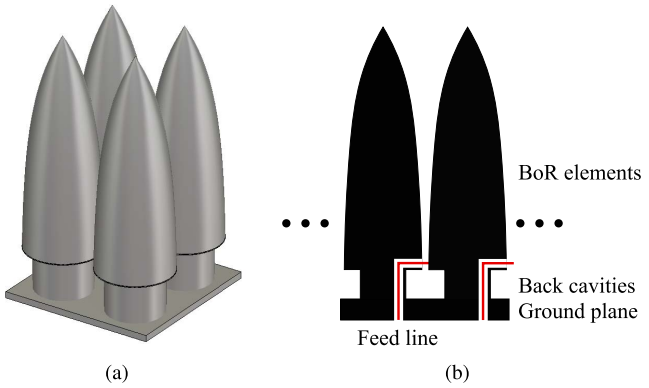

FIGURE 1. (a) 3-D view and (b) cross section of conventional BoR antenna elements. Adapted from [7].

types have been developed, such as the body-of-revolution (BoR) array [2], the balanced antipodal Vivaldi array [3], the bunny-ear array [4], and several all-metal flared-notch arrays [5], [6]. The Vivaldi-type elements can offer very high bandwidths, even larger than 10:1, depending on the shape and feeding arrangement of the elements.

In 2003, H. Holter introduced the axially symmetric BoR element [7], whose main advantages are the rigid, easily manufacturable all-metal structure, modularity, and easy maintenance [2], [7]. In addition, due to the axially symmetric shape of the element, a dual-polarized operation is easy to implement. They have been shown to provide similar performance characteristics to corresponding PCB-based Vivaldi arrays, but with lower losses [2].

Fig. 1 shows the structure of a conventional BoR array. The array consists of four functional parts: BoR elements, back cavity, ground plane, and feed network. The back cavity under the opening of the tapered slotline transforms the unbalanced coaxial feed to a balanced one. Therefore, the shape and size of the back cavity are crucial from the impedance bandwidth point of view. In the designs presented in [2] and [7], the cavity was designed such that the current null is placed in its middle. Thus, the contact quality between the elements is insignificant, and the modularity of the antenna array is guaranteed.

Despite the many desirable properties of the conventional BoR array, they also have some disadvantages. In [2] and [7], the arrays were made of solid metal, thus making them heavy. In addition, all the BoR elements and the chassis on which the elements are attached, are manufactured through industrial machinery. This is feasible, but the machinery and assembly of the BoR antenna array is an expensive and time-consuming process.

To overcome the disadvantages of the conventional BoR array, a possible solution to lighten and simplify the antenna structure was presented and patented in [8]. The main idea in this solution is to make an inverted BoR structure, where BoR-shaped elements are formed in a dielectric block by manufacturing cavities (e.g., by milling or drilling) and metalizing their surface from the inside. The design is more

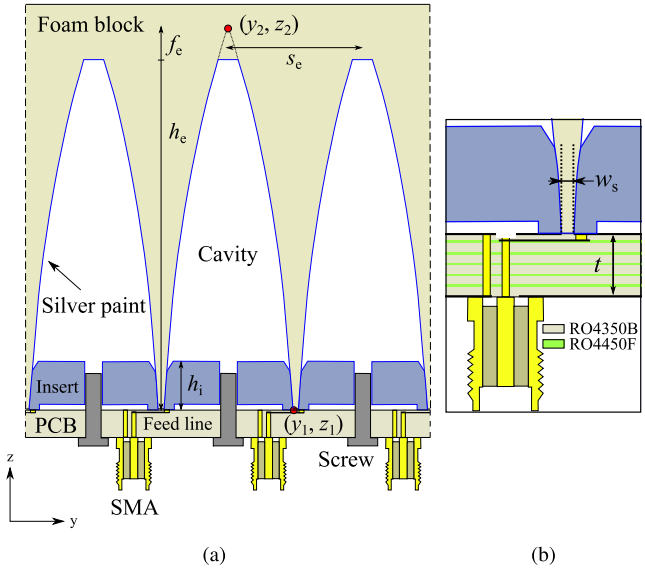

FIGURE 2. (a) Cross section of the proposed inverse BoR phased array. (b) Detailed view on the junction of the PCB and the foam block.

lightweight, robust, and much simpler to manufacture than a conventional BoR array. Furthermore, these properties result in significantly lower manufacturing costs.

In addition to the inverted BoR structure, we propose a feed design where all parts are integrated into a PCB, including the back cavity. The original idea of the integrated feeding system has been developed in conjunction with the inverted BoR structure and patented in [9]. The main advantage of the proposed design is that all parts needed for feeding the antenna elements are included in a single 5-mm-thick PCB, and the shape of the actual element can be kept simple. The manufacturing process of the PCB-integrated feeding system is considerably simpler than that of conventional all-metal designs, like those in [2], [5].

This paper is constructed as follows: In Section II, the structure of the inverted BoR array is presented in detail. Section III proceeds with the simulation and measurement results of the designed inverted BoR array, after which Section IV concludes the paper.

II. ANTENNA STRUCTURE AND MANUFACTURING TECHNIQUES

Fig. 2 shows the cross section of the proposed dual-polarized inverted BoR array. The structure consists of three functional layers: a metalized foam block, inserts, and a PCB. The BoR elements are formed by milling cavities in the foam block and then metalizing their inner surface. Metalized, plastic inserts make a galvanic connection between the metalized surface of the cavities and the surface of the PCB. The PCB includes the feeding network of the antenna elements. A detailed description of each part is provided in the following sections.

The manufactured array has 6×6 BoR cavities, corresponding to 5×6 antenna elements. The physical area of

TABLE 1. Dimensions of the proposed antenna.

Parameter	Description	Value
h_e	Height of the element	65 mm
d_e	Bottom diameter of the element	24 mm
s_e	Element spacing	25 mm
f_e	Flattening of the tip	5 mm
h_i	Height of the insert	9 mm
t	Thickness of the PCB	5 mm
w	Width of the stripline	1 mm
w_s	The width of the tapered slotline	1 mm
l	Length of the stripline	6.1 mm
R	Exponential curve parameter	0.025

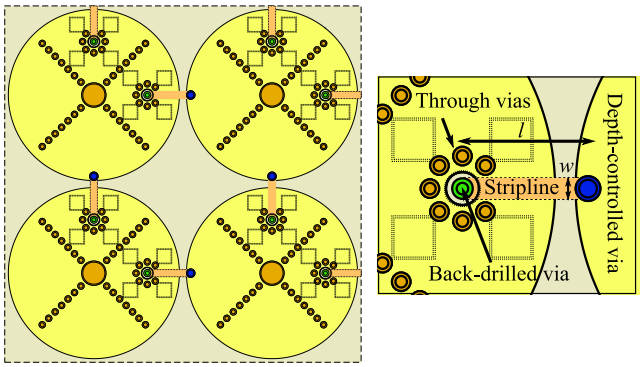

(a) (b)

FIGURE 3. (a) Illustration of the conductors and vias in the PCB (top view) and (b) a close up of a single antenna feed. The inner layer is drawn with a dashed line.

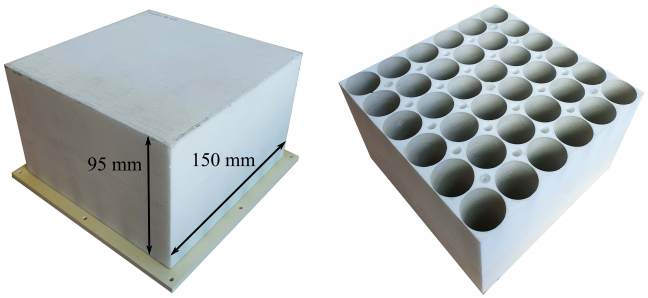

(a) (b)

FIGURE 4. Manufactured antenna array. (a) Assembled array, (b) painted cavities in the foam.

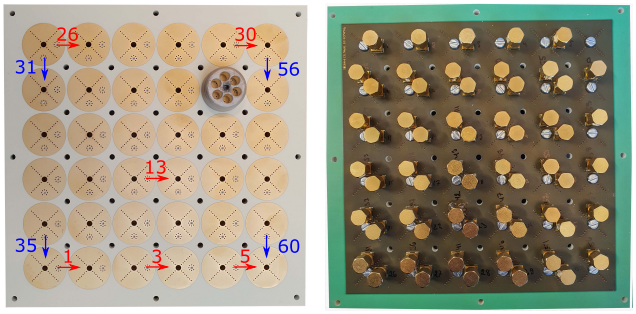

(a) (b)

FIGURE 5. Manufactured PCB: (a) Top surface with one insert attached, (b) bottom surface with SMA connectors and 50-ohm terminations. Element numbers of different polarizations are marked with separate colors and the arrows designate the direction of the E-field. The size of the PCB is 170 mm × 170 mm.

the array is $\lambda_{low} \times \lambda_{low}$, λ_{low} being the wavelength at the lowest frequency, which is 2 GHz. However, [10] suggests that the size of an array should be at least $5\lambda_{low} \times 5\lambda_{low}$ so that the behaviour of the center element matches that of the element of an infinite array in unit-cell simulations. Since manufacturing and characterization of such a large array (30 × 30 BoR cavities) is increasingly laborious, we limit the array size to 6 by 6 cavities.

A. PRINTED CIRCUIT BOARD

Figs. 2 and 3 illustrate the PCB underneath the foam. The SMA connector under the PCB is soldered directly to the via that connects the inner conductor of the SMA connector to the stripline inside the PCB. The wave that propagates along the microstrip line is coupled through the electromagnetic fields to the first cavity and galvanically to the second one. Thus, the dimensions of the line, and the separation between the microstrip line and the upper copper layer, define the strength of the coupling.

In the original BoR design, the balun was implemented using a back cavity behind the tapered slotline [2]. This method is robust and wideband but requires expensive, milled parts. In the proposed design, the back cavity is integrated into the PCB. In order to achieve sufficient impedance bandwidth, a 5-mm-thick PCB with a low-loss Rogers RO4350B substrate is used. Based on our experience, a thicker substrate leads to a wider band.

In contrast to the traditional design, the back cavity is formed with cross-shaped via fences under each element (see Fig. 3). In addition, due to the limited thickness of the PCB, the back cavity is wider. The cross-shaped via fences should extend to the edges of the circular pad on the top layer, which reduces the mutual coupling between ports of different polarizations and also prevents undesired internal resonances inside the PCB. However, if the via fences were too close to edges, they would limit the size of the back cavity and thus narrow the impedance bandwidth. In other words, the size of the via fences is a compromise between impedance bandwidth and awakening of non-desired internal resonances.

The used substrate, Rogers RO4350B, has a relative permittivity of 3.66 and loss tangent of 0.0037 at 10 GHz. Because the dimensions of the back cavity depend on the wavelength, the height of the PCB can be further reduced by using a higher-permittivity substrate material. As a consequence, this would also reduce the bandwidth due to larger reflections in the substrate-Vivaldi interface.

B. FOAM BLOCK

The elements of the inverted BoR antenna are manufactured by milling cavities in the dielectric foam block and metallizing their inside. The bottom diameter of the elements is

24 mm and the tapering is defined by an exponential curve given by [11]

$$y = c_1 e^{Rz} + c_2, \tag{1}$$

where

$$c_1 = \frac{y_2 - y_1}{e^{Rz_2} - e^{Rz_1}}, \tag{2}$$

$$c_2 = \frac{y_1 e^{Rz_2} - y_2 e^{Rz_1}}{e^{Rz_2} - e^{Rz_1}}. \tag{3}$$

Here, R is a parameter defining the shape of the exponential curve. Constants y_1, y_2, z_1, and z_2 are coordinate points illustrated in Fig. 2.

The element spacing of 25 mm is half of the wavelength at 6 GHz, which is the highest frequency. Thus, no grating lobes appear when the scan angle $\theta < 90°$ [12]. With a 24-mm element diameter, the slot width in the opening of the tapered slotline is 1 mm. A slightly narrower slot would be better from the impedance matching point of view, but then the decreased strength of the walls between the cavities might cause manufacturing and robustness problems.

The height of the elements is 65 mm, which corresponds to $0.43\lambda_{\text{low}}$ or $1.3\lambda_{\text{high}}$. In general, a higher element results in a larger bandwidth by extending the lower band edge to the lower frequency. However, a higher element also results in poorer polarization performance in the diagonal plane [13].

Since there is dielectric material between the elements, special attention should be paid to the losses and dielectric permittivity of the foam. In order to minimize losses and the effect of the foam, a low-loss, low-permittivity foam is selected. Several possible materials have successfully been used to manufacture lightweight microwave components and antennas [14]–[16]. In the proposed design, we use Rohacell 71 HF due to its relatively rigid closed-cell structure, good workability, and excellent microwave characteristics. Its dielectric constant and loss tangent are 1.09 and 0.0038 at 10 GHz, respectively. A higher-permittivity dielectric material could also be used to reduce the dimensions of the antenna, but this may negatively affect the matching and impedance bandwidth.

In addition to the dielectric material, the metalization of the cavities is crucial for the performance of the antenna. Three parameters affect the overall radiation efficiency of the antenna: surface roughness on the inside of the cones, metal conductivity, and metal thickness. Metalization can be applied by several methods, such as vacuum metalization, chemical plating, and conductive painting. In order to obtain a selective coating with sufficient conductivity, we chose MG Chemicals 842WB Super Shield conductive paint, which provides a resistivity of $7.5 \cdot 10^{-5}\ \Omega \cdot \text{cm}$ that gives excellent surface conductivity even with 25-μm film thickness [17]. The surface can be painted either with a brush or a spray gun. However, due to the nature of machined foam material, the surface is inherently rough. The roughness cannot be accurately defined without measurements since it depends on both machining quality and the cell size of the foam material.

TABLE 2. Measured masses of the manufactured parts, and estimated masses of conventional BoR arrays made of 3-D printed plastic and solid aluminum.

Antenna array	Parts	Mass (g)	Total (g)
This work	Foam block, height 95 mm	130	517
	3-D printed inserts	99	
	PCB	288	
Plastic array	3-D printed hollow cones	420	708
	PCB	288	
All-metal array	Solid cones (Al)	1500	1890
	Back plane (Al)	390	

In the manufactured prototype, the conductive paint was applied with a regular paintbrush. Based on the paint consumption, we estimate that the film thickness is 50–150 μm, corresponding to a thickness of 5–15 skin depths at 2 GHz. On this basis, the film is thick enough to provide good radiation efficiency. Thus, losses due to the metalization are mainly caused by the finite conductivity of the paint and the surface roughness.

C. INSERTS

A galvanic contact between the cones and the PCB is established using inserts. In order to reduce the weight of the antenna structure, the inserts are made of 3-D printed plastic that is painted with conductive paint. The RF properties of the plastic are unimportant since the whole insert is covered with conductive paint. The shape and size of the inserts are precisely adjusted to fit into cone-shaped cavities. Fig. 2 shows the dimensions and the cross section of the inserts.

D. WEIGHT

One of the design targets was to reduce the weight of the conventional BoR antenna. Table 2 summarizes the masses measured for the manufactured inverted BoR array and calculated for other types of arrays. In general, the inverted structure is the lightest because is does not contain solid metal parts. A significant reduction of mass can be obtained also by manufacturing conventional cones from plastic and metalizing them on the outside. However, the plastic structure is still heavier than the inverted one. The conventional all-metal structure, where the cones and the back plane are manufactured from metal, results in the heaviest set. This structure is over three times heavier than the inverted one.

III. SIMULATION AND MEASUREMENT RESULTS

A. INFINITE ARRAY SIMULATIONS

The infinite array simulations were conducted in CST Studio Suite 2021 using the unit-cell (UC) boundary condition [18]. The simulated active reflection coefficient (ARC) is shown in Fig. 6, where the ARC is shown for the H-, E-, and D-planes separately. The H- and E-planes refer to the principal planes in parallel with the magnetic and electric field vectors, respectively. The D-plane is the diagonal plane between the H- and E-planes. The simulation results show

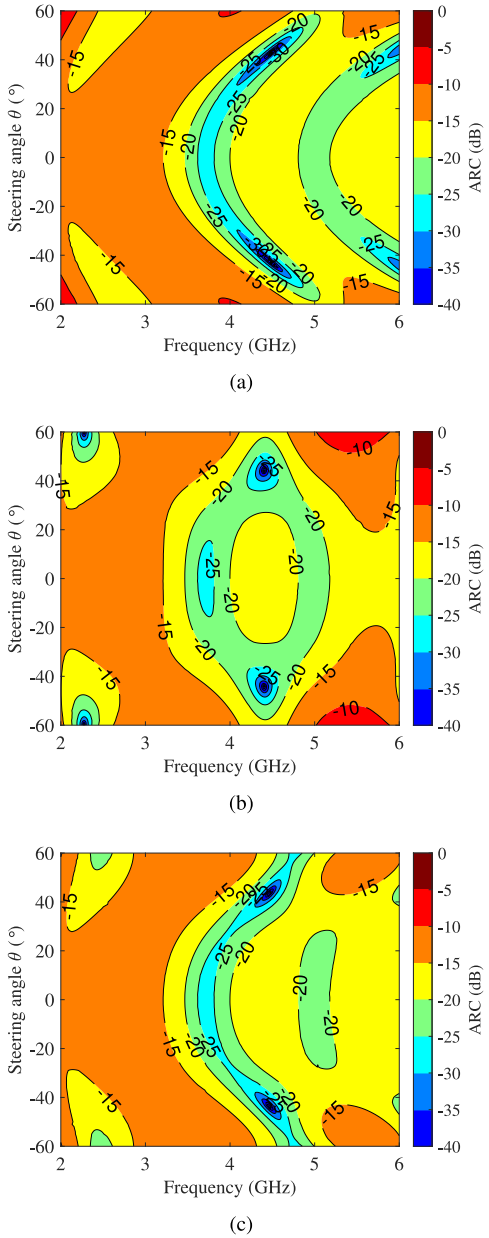

FIGURE 6. Simulated ARC of an infinite array in the (a) H-plane, (b) E-plane, and (c) D-plane.

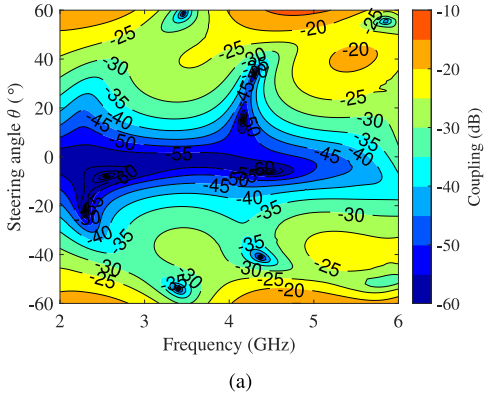

FIGURE 7. Simulated (UC) cross coupling between the feed ports when the beam is steered in the D-plane.

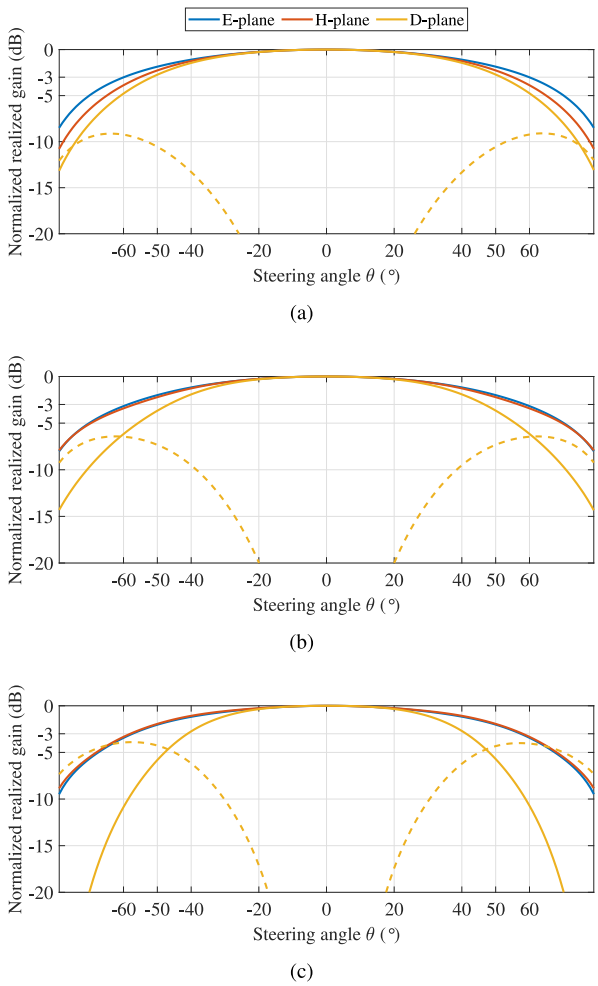

FIGURE 8. Active element pattern of an infinite array at (a) 2 GHz, (b) 4 GHz, and (c) 6 GHz. Co-polarization is denoted by solid line and cross-polarization with dashed line. Cross-polarization levels in the E- and H-plane are negligible and not shown in the figure.

that the impedance matching level is better than −10 dB for ±50° beam steering range in all planes.

Fig. 7 shows the cross coupling when the beam is steered in the D-plane. The coupling in the principal planes is negligible and not shown here. Generally, the coupling is small also in the D-plane, but it increases near 6 GHz due to internal resonances which emerge at that frequency in the PCB.

Fig. 8 shows the active element pattern (AEP) of an infinite array. In the ±50° beam-steering range, the scan loss is less than 3 dB in the principal planes. The AEP follows approximately the ideal gain pattern defined by

$$g_{\mathrm{ro}}(\theta,\phi) = \frac{4\pi A}{\lambda^2}\cos\theta(1-|\Gamma(\alpha,\beta)|^2), \tag{4}$$

where θ and ϕ are scan angles in the spherical coordinate system, A is the effective area of one element, λ is the wavelength, α and β are the element phasings for rows and columns, respectively, and Γ is the ARC [19]. However, in the diagonal planes, the co-polarized component

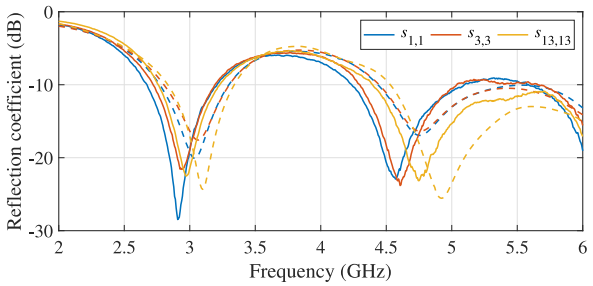

FIGURE 9. Measured (solid line) and simulated (dashed line) reflection coefficients of a 5 × 6 finite array. Element 1 is located in the corner, 3 in the edge midpoint, and 13 in the center of the array, as depicted in Fig. 5.

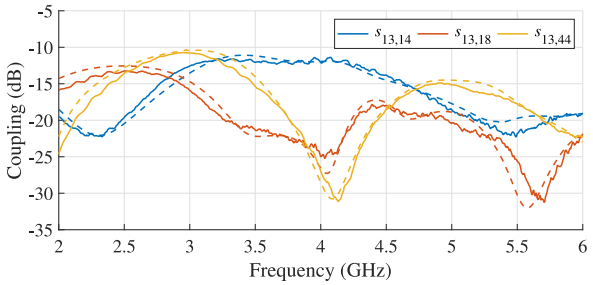

FIGURE 10. Measured (solid line) and simulated (dashed line) coupling coefficients of a 5×6 finite array. Parameters $s_{13,14}$ and $s_{13,18}$ describe the coupling between adjacent elements in the E- and H-plane, respectively, and $s_{13,44}$ depicts the coupling between different polarizations.

degrades significantly with increasing frequency. At 6 GHz, only a ±40° beam-steering range is possible with 3 dB scan loss criterion. The high cross-polarization level is a common disadvantage of Vivaldi-type arrays, especially when the element height is large compared to the wavelength [13]. Nevertheless, this property can be compensated with optimized feeding coefficients [20].

B. FINITE ARRAY SIMULATIONS AND MEASUREMENTS

1) S-PARAMETERS

The operation of the manufactured array was confirmed with S-parameter measurements. Not all S-parameters, but the most significant ones, were measured and compared to the full-array simulation results. Fig. 9 shows the measured reflection coefficients of the center, edge, and corner elements. The resonance peaks of these elements are at a lower frequency than those of the simulated ones. This small, 100–200-MHz shift in frequency is due to the uncertainty in the permittivity of the materials or manufacturing tolerances. Nevertheless, the simulated and measured reflection coefficients match very well and, most importantly, the array operates as intended.

Fig. 10 shows the coupling between adjacent elements, and also between the polarizations. Again, the measurement results show good agreement with the simulations. Notably, the frequency shift is not as clearly visible as in the reflection coefficient.

Note that the reflection and coupling coefficients of single elements do not describe exactly the operation of the array in a real-use scenario. With simultaneous excitation, the ARCs and coupling vary depending on the amplitudes and phases of the excitation.

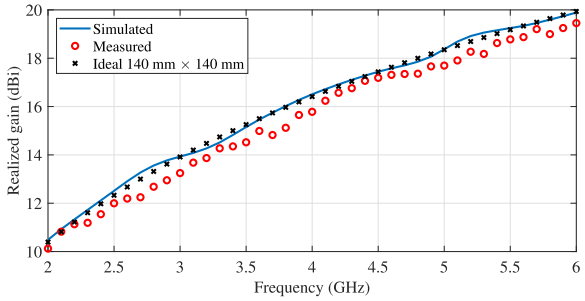

FIGURE 11. Realized gain of the 5×6 array in the broadside direction. The simulation results neglect the losses of the cavity metalization. The ideal gain is based on (4), where a 140 mm×140 mm aperture is assumed and the impedance mismatch is omitted.

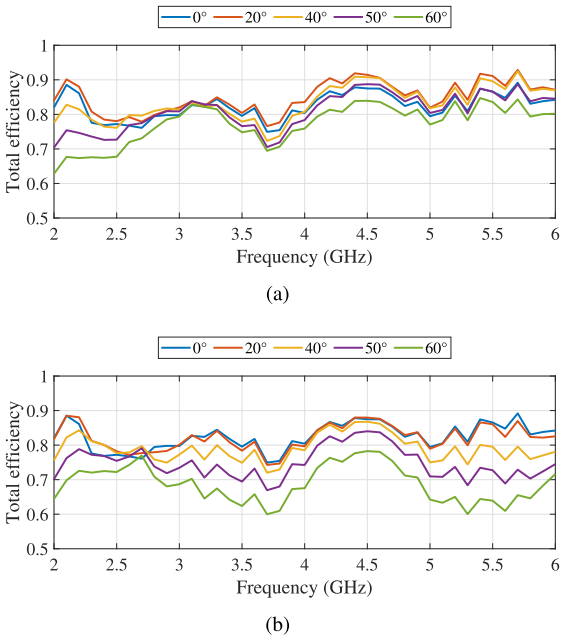

FIGURE 12. Measured total efficiency, when the beam is steered in the (a) H-plane and the (b) E-plane.

2) ARRAY GAIN, RADIATION PATTERN, AND EFFICIENCY

The far fields and related parameters are measured using the MVG StarLab 6 GHz system. All ports of one polarization are measured separately.

The far-field pattern of the manufactured 5×6 array can be computed numerically by combining all measured individual element patterns as in [21]–[23]:

$$\boldsymbol{F}(\theta,\phi)_{\text{array}} = \sum_{n=1}^{N} a_n \boldsymbol{F}_n(\theta,\phi), \tag{5}$$

where $\boldsymbol{F}_n$ is the measured electric far-field data of the n^{th} element, a_n is the corresponding excitation coefficient, and N is the number of elements to be excited. The phase differences caused due to the relative locations of the elements

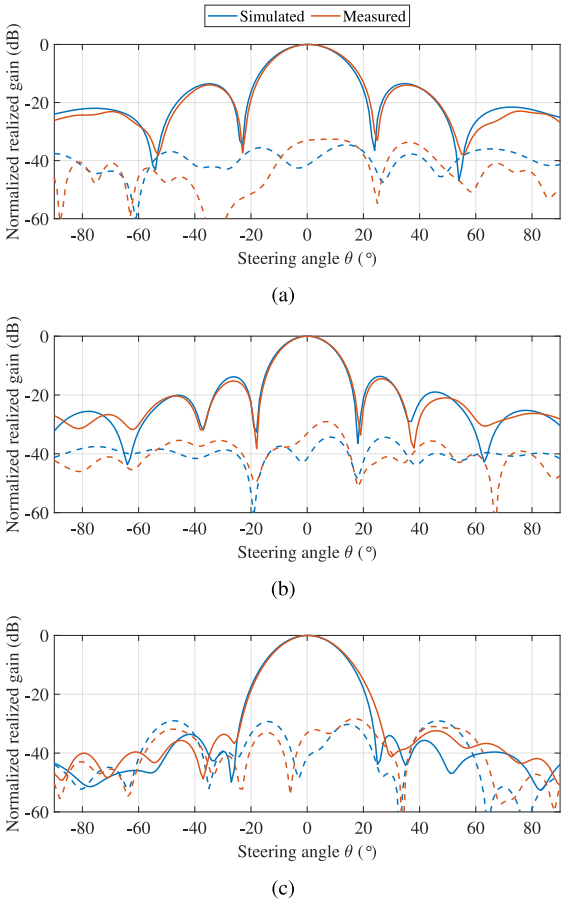

FIGURE 13. Array pattern at 6 GHz in the (a) E-, (b) H-, and (c) D-planes. Co-polarization is denoted by a solid line and cross-polarization with a dashed line.

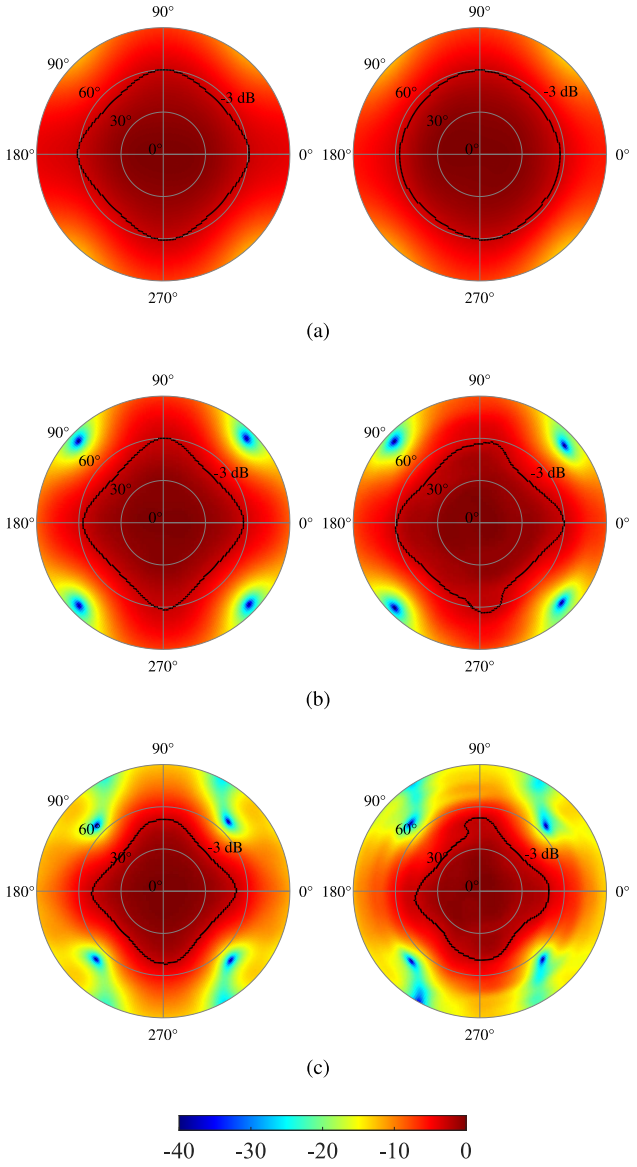

FIGURE 14. Simulated (left) and measured (right) normalized co-polarization patterns at (a) 2 GHz, (b) 4 GHz, and (c) 6 GHz.

are already included in the measurement data. The excitation coefficients are normalized such that

$$\sum_{n=1}^{N} |a_i|^2 = 1. \tag{6}$$

Using the StarLab measurement data, the radiation intensity can be computed from the θ and ϕ components of (5) as

$$U(\theta, \phi) = B_0(|\boldsymbol{F}^{\theta}_{\text{array}}(\theta, \phi)|^2 + |\boldsymbol{F}^{\phi}_{\text{array}}(\theta, \phi)|^2), \tag{7}$$

where B_0 is a calibration and normalization coefficient obtained from the measurement device [23]. Then, the total efficiency of the antenna array is the ratio of the radiated power to the available power:

$$\eta_{\text{tot}} = \frac{P_{\text{rad}}}{P_{\text{avail}}} = \int_0^{2\pi} \int_0^{\pi} U(\theta, \phi) \sin\theta \mathrm{d}\theta \mathrm{d}\phi. \tag{8}$$

Using (5) and (6), the realized gain of the array with uniform excitation in the broadside direction is calculated and shown in Fig. 11. The figure shows that the simulation and measurements results agree well at all frequencies. The lower realized gain of the manufactured antenna is probably mainly due to conduction losses in the cavity metalization. On average, the measured realized gain is 0.53 dB lower than the simulated one, resulting in an additional 11% loss in radiation efficiency. Fig. 11 also shows the ideal gain of an array with a 140 mm×140 mm aperture, computed with (4). The impedance mismatch is neglected.

Fig. 12 presents the measured total efficiency of the array at different steering angles. The total efficiency is computed numerically from the far-field measurement data using (8). In general, the array exhibits a total efficiency of 0.7–0.9, depending on the frequency and steering angle. In full-array simulations, the total efficiency is 0.9–1.0 in the broadside direction, when the losses in cone metalization are neglected. This result is in line with the realized gain measurements, where the results showed 11% reduction in the realized gain. Furthermore, the results show a significant reduction in the total efficiency in the E-plane when the beam is steered towards 60°. Obviously, this is mainly caused by

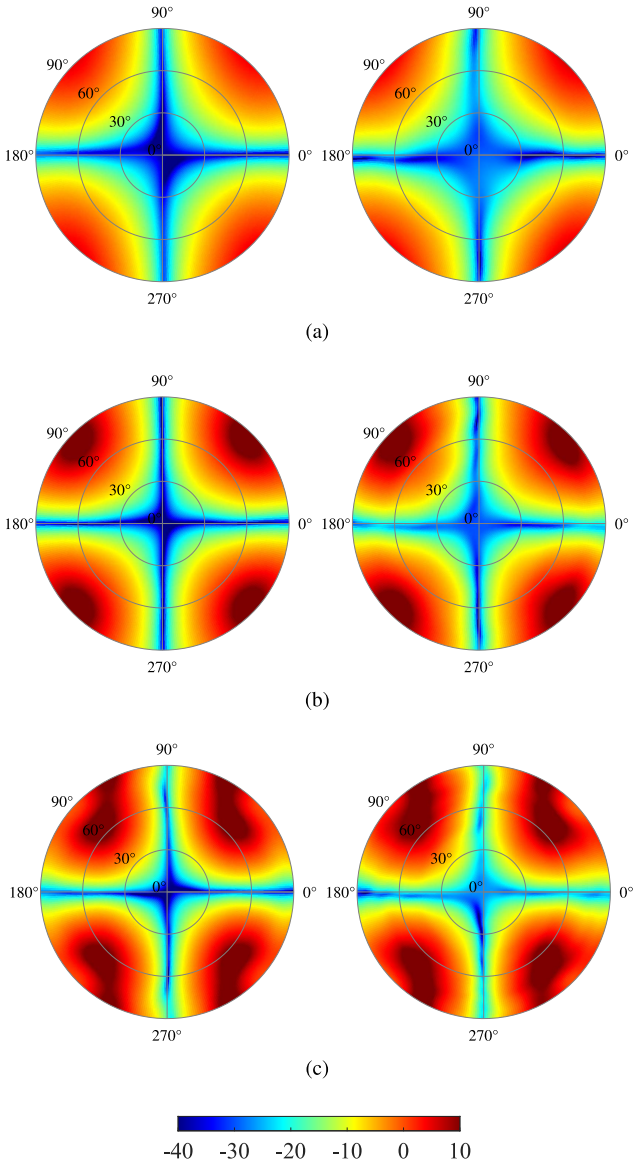

FIGURE 15. Simulated (left) and measured (right) CPR at (a) 2 GHz, (b) 4 GHz, and (c) 6 GHz.

the deteriorated impedance matching. In the H-plane, the total efficiency is better.

Fig. 13 shows the co- and cross-polarization components of the array pattern in the broadside direction in the E-, H-, and D-planes, respectively. In the H-plane, the main beam is narrower due to the larger effective aperture. The measurement results are in line with the simulations.

3) POLARIZATION PURITY

The polarization purity of typical Vivaldi-type antennas is known to be excellent on the principal planes but significantly worse on the diagonal plane [13]. Fig. 14 shows the co-polarized active element pattern of the finite array. The results are obtained by computationally steering the beam of a 5×6 finite array and observing the electric field from the theoretical beam-steering direction. The measurement results

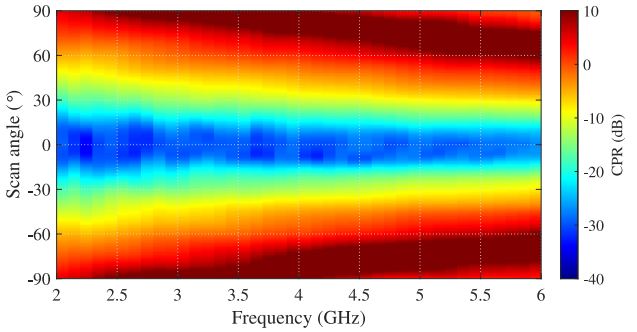

FIGURE 16. Measured CPR in the diagonal plane.

show a good correspondence with the simulated patterns and the infinite array patterns in Fig. 8.

Fig. 15 shows the cross-polarization ratio (CPR) of the manufactured finite array as a function of the steering angle. The CPR, the cross-polarized component divided by the co-polarized component (on a linear scale), takes into account both co-polarization and cross-polarization levels. The measurement results show an excellent agreement with the simulations. As expected, the CPR is excellent on principal planes but degrades significantly when the beam is steered in the diagonal planes. On the upper end of the frequency scale, the length of the elements is large compared to the wavelength, which degrades the polarization performance. This effect is better illustrated in Fig. 16, where the CPR is presented in the diagonal plane as a function of frequency.

IV. CONCLUSION

A dual-polarized antenna array with inverted BoR elements is designed and characterized. This manufacturing technique, where antenna elements are formed inside a foam material, was shown to be realizable. In addition, the performance characteristics of the antenna are comparable to those of the conventional BoR array whereas the cost and weight of the presented array are significantly reduced.

The designed antenna provides 3:1 impedance bandwidth with an ARC<-10 dB. The bandwidth is maintained for a 50° scan in all planes. However, the polarization purity of the antenna is typical of Vivaldi-type arrays, being relatively poor for large scan angles in the D-plane, but this inferiority can be mitigated with optimized feeding [20]. The measured total efficiency of the antenna is 0.7–0.9, depending on the frequency. The comparison with the simulation results suggests that the additional loss in the manufactured prototype is mainly caused by the metalization of the antenna elements, and the loss in the PCB has a minor effect.

Nevertheless, due to its significantly reduced weight, cost, and complexity, the array is an attractive option for applications where low-cost and lightweight arrays are needed, e.g., in unmanned aerial vehicles and telecommunications. Furthermore, the volume inside the cavities can be exploited for integrating electronics or passive components, such as filters. This might be a significant advantage if the overall height of the system can be reduced with a higher integration rate.

ACKNOWLEDGMENT

The authors would like to thank Mr. Antti Kuhlberg for assisting with the manufacturing of the antenna. In addition, thanks go to Mr. Stefan Andersson for conducting the antenna measurements. The research is conducted in a collaboration between Aalto University and Saab AB.

REFERENCES

[1] P. Gibson, "The Vivaldi aerial," in *Proc. 9th Eur. Microw. Conf.*, 1979, pp. 101–105.
[2] H. Holter, "Dual-polarized broadband array antenna with BOR-elements, mechanical design and measurements," *IEEE Trans. Antennas Propag.*, vol. 55, no. 2, pp. 305–312, Feb. 2007.
[3] M. W. Elsallal and J. C. Mather, "An ultra-thin, decade (10:1) bandwidth, modular 'BAVA' array with low cross-polarization," in *Proc. IEEE Int. Symp. Antennas Propag. (APSURSI)*, 2011, pp. 1980–1983.
[4] J. Lee, S. Livingston, and R. Koenig, "A low-profile wide-band (5:1) dual-pol array," *IEEE Antennas Wireless Propag. Lett.*, vol. 2, pp. 46–49, 2003.
[5] R. W. Kindt and W. R. Pickles, "Ultrawideband all-metal flared-notch array radiator," *IEEE Trans. Antennas Propag.*, vol. 58, no. 11, pp. 3568–3575, Nov. 2010.
[6] H. Kähkönen, J. Ala-Laurinaho, and V. Viikari, "Dual-polarized Ka-band Vivaldi antenna array," *IEEE Trans. Antennas Propag.*, vol. 68, no. 4, pp. 2675–2683, Apr. 2020.
[7] H. Holter, "A new type of antenna element for wide-band wide-angle dual polarized phased array antennas," in *Proc. IEEE Int. Symp. Phased Array Syst. Technol.*, 2003, pp. 393–398.
[8] S. Gunnarsson and J. Malmström, "Inverted antenna elements," World Patent 101 424 A1, May 27, 2021.
[9] S. Gunnarsson and J. Malmström, "A feeding system for an array of BoR antenna elements," World Patent 101 425 A1, May 27, 2021.
[10] H. Holter and H. Steyskal, "On the size requirement for finite phased-array models," *IEEE Trans. Antennas Propag.*, vol. 50, no. 6, pp. 836–840, Jun. 2002.
[11] J. Shin and D. Schaubert, "A parameter study of stripline-fed Vivaldi notch-antenna arrays," *IEEE Trans. Antennas Propag.*, vol. 47, no. 5, pp. 879–886, May 1999.
[12] W. L. Stutzman and G. A. Thiele, *Antenna Theory and Design*, 3rd ed. Hoboken, NJ, USA: Wiley, 2012.
[13] J. T. Logan, R. W. Kindt, M. Y. Lee, and M. N. Vouvakis, "Opportunities and advances in ultra-wideband electronically scanned arrays," in *Proc. IEEE Int. Symp. Antennas Propag. (APSURSI)*, 2016, pp. 431–432.
[14] J.-P. Coupez and C. Person, "Metallized 3D foam technology: A well-suited solution for high performance, low-cost, CM-wave and MM-wave system integration," in *Proc. 15th Int. Conf. Microw. Radar Wireless Commun.*, vol. 2, 2004, pp. 379–390.
[15] S. Chenu, J.-P. Coupez, F. Karpus, and B. Toublanc, "Development of new technologies using foam materials for RF device integration," in *Proc. Eur. Microw. Conf.*, 2013, pp. 326–329.
[16] A. Rolland, N. T. Nguyen, R. Sauleau, C. Person, and L. Le Coq, "Smooth-walled light-weight Ka-band shaped horn antennas in metallized foam," *IEEE Trans. Antennas Propag.*, vol. 60, no. 3, pp. 1245–1251, Mar. 2012.
[17] *842WB Liquid EMI Conductive Paint*, 842WB Liquid Datasheet, MG Chemicals, Surrey, BC, Canada, Aug. 2021.
[18] M. Rütschlin, T. Wittig, and Z. Iluz, "Phased antenna array design with CST studio suite," in *Proc. 10th Eur. Conf. Antennas Propag. (EuCAP)*, 2016, pp. 1–5.
[19] P. Hannan, "The element-gain paradox for a phased-array antenna," *IEEE Trans. Antennas Propag.*, vol. 12, no. 4, pp. 423–433, Jul. 1964.
[20] R. Kindt and D. Taylor, "Polarization correction in dual-polarized phased arrays of flared notches," in *Proc. IEEE Int. Symp. Antennas Propag. (APSURSI)*, 2011, pp. 1961–1964.
[21] J. Allen, "Gain and impedance variation in scanned dipole arrays," *IRE Trans. Antennas Propag.*, vol. 10, no. 5, pp. 566–572, 1962.
[22] D. Pozar, "The active element pattern," *IEEE Trans. Antennas Propag.*, vol. 42, no. 8, pp. 1176–1178, Aug. 1994.
[23] J.-M. Hannula, T. Saarinen, J. Holopainen, and V. Viikari, "Frequency reconfigurable multiband handset antenna based on a multichannel transceiver," *IEEE Trans. Antennas Propag.*, vol. 65, no. 9, pp. 4452–4460, Sep. 2017.